electronic reprint

JOURNAL OF APPLIED CRYSTALLOGRAPHY

ISSN: 1600-5767
journals.iucr.org/j

Influence of solidification history and particle size on defect evolution in Al2024 alloy additive manufacturing powder

Colby Azersky, Sangho Jeon, Matthias Kolbe, Caitlin Walde and Douglas Matson

J. Appl. Cryst. (2026). **59**, 1384–1392

IUCr Journals
CRYSTALLOGRAPHY JOURNALS ONLINE

Author(s) of this article may load this reprint on their own web site or institutional repository and on not-for-profit repositories in their subject area provided that this cover page is retained and a permanent link is given from your posting to the final article on the IUCr website.

For further information see https://journals.iucr.org/services/authorrights.html

JOURNAL OF APPLIED CRYSTALLOGRAPHY

ISSN 1600-5767

Influence of solidification history and particle size on defect evolution in Al2024 alloy additive manufacturing powder

Colby Azersky,[a]* Sangho Jeon,[b] Matthias Kolbe,[c] Caitlin Walde[d] and Douglas Matson[e]

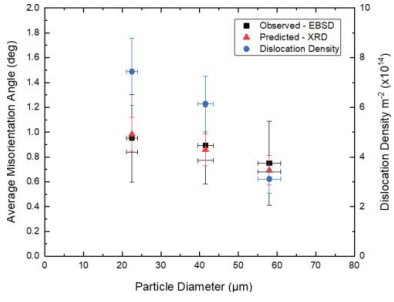
[a]Goddard Space Flight Center, National Aeronautics and Space Administration, Greenbelt, MD 20771, USA, [b]Deutsches Elektronen-Synchrotron (DESY), Notkestraße 85, D-22607 Hamburg, Germany, [c]German Aerospace Center (DLR), Linder Höhe, D-51147Cologne, Germany, [d]Solvus Global, 104 Prescott Street, Worcester, MA 01605, USA, and [e]Department of Mechanical Engineering, Tufts University, Medford, MA 02155, USA. *Correspondence e-mail: colbyazersky@gmail.com

Received 7 March 2024
Accepted 26 June 2026

Edited by H. Brand, Australian Synchrotron, ANSTO, Australia

Keywords: Al2024 alloy; dislocation density; X-ray line profile analysis; electron backscatter diffraction; additive manufacturing; solidification.

This study investigates the impact of solidification history on defect evolution in Al2024 alloy additive manufacturing powder. A measurement utilizing synchrotron powder X-ray diffraction (XRD) was performed with a photon energy of 105.7 keV (0.1173 Å). XRD measurements were completed for six distinct particle diameter ranges from 20 to 63 µm of both as-atomized and annealed Al2024 samples. The dislocation density was determined using X-ray line profile analysis and ranged between 3.1×10^{14} and 7.4×10^{14} m^{-2} for as-atomized samples, and between 1.3×10^{14} and 4.0×10^{14} m^{-2} for annealed samples. The results of this investigation suggest a trend of decreasing dislocation density in as-atomized samples as the particle size increases, demonstrating the influence of particle size on defect formation. The annealed samples show a weak size dependence on the dislocation density across all particle sizes, affirming the efficacy of the annealing process in healing microstructural defects. The reduction in dislocation density upon annealing confirms that the dislocations in the as-atomized samples were introduced during rapid solidification and are largely removed by heat treatment. Field-emission scanning electron microscopy and electron backscatter diffraction (EBSD) were used in conjunction with image analysis tools to quantify the grain interface areas of the as-atomized samples and estimate cooling rates during solidification. Cooling rates were found to vary with particle size within a range of roughly 22000 to 164000 K s^{-1}. Results from both XRD analysis and metallography were used to predict average misorientation angles between grains; the predicted angles range from roughly 0.68° to 0.83°. EBSD was utilized to quantify average misorientation angles and compare them with the predicted values. The EBSD measured angles ranged from roughly 0.74° to 0.95° and followed the same trend as the predictions, linking the dislocation density to the cooling rate and solidification history of the powder. Quantifying the dislocation density and average misorientation angle provides a deeper understanding of the microstructure produced during rapid solidification. These results establish a physical relationship between particle size, cooling rate, dislocation density and grain misorientation during rapid solidification of Al2024 powder. This relationship is relevant to the study of solidification and to applications where gas-atomized powder is utilized without necessarily being fully remelted.



1. Introduction

Understanding the recrystallization process and resulting microstructural defects present in rapidly solidified alloys is central to relating solidification history to the resulting defect structure. This study investigates the impact of solidification history on defect evolution in the 2024 aluminium alloy (Al2024). Al2024 was chosen as the model material for this set of experiments due to its excellent material properties and

electronic reprint

widespread use in industry, especially in aviation and aerospace applications (Zhan *et al.*, 2021). Specifically, excellent strength, fatigue resistance and damage tolerance, and high fracture toughness, along with its emerging use in additive manufacturing (AM), make Al2024 a strong candidate for further research (Pekok *et al.*, 2021). Gas-atomized Al2024 manufacturing powder was utilized because the manufacturing process generates a distribution of individual particle sizes. Variations in particle size allow for a variety of solidification histories to be studied because the cooling rate is a function of particle size (Henein *et al.*, 2017). Typical diameter ranges for powder particles utilized in powder bed fusion (PBF) processes range from roughly 25 to 60 µm (Gallagher *et al.*, 2023). Given the differences in cooling rate across the size range, it is important to understand the relationship between particle size and dislocation density to give proper control over subsequent consolidation operations. In fusion-based processes such as PBF, the as-atomized defect structure is reset to the extent that the powder is fully remelted. The relationships reported in this work are therefore most relevant to solidification science and to processes where full remelting does not occur, such as cold spray additive manufacturing, where the as-atomized defect structure persists and shapes the final microstructure rather than being lost to melting.

While comprehensive analysis has not yet been conducted on raw Al2024 AM powder, research has been conducted on the dislocation density of powders of other materials, such as $AlCrFe_2Ni_2$ (Jeon *et al.*, 2021) and Inconel 718 (Azersky *et al.*, 2023), and other as-built AM structures using gas-atomized powders (Prasad *et al.*, 2021; Brown *et al.*, 2017). Prasad *et al.* (2021) utilized AM Inconel 718 manufactured from powders with diameters between 10 and 45 µm. Brown *et al.* (2017) utilized AM SS 304L manufactured from powders with diameters between 44 and 105 µm. Dislocation density analysis performed in these studies yielded results within the range of 10^{13} to 10^{15} m^{-2}.

Dislocations in nanocrystalline materials generate microstrain in the atomic lattice (Ungár, 2001); this strain can be quantitatively analyzed using X-ray diffraction line profile analysis techniques (Zhang *et al.*, 2020; Ungár & Borbély, 1996; Ungár *et al.*, 1998; Tong *et al.*, 2015; Martinez-Garcia *et al.*, 2009). Specifically, these methods were applied to analyze the strain broadening of Bragg peaks within the profile due to the dislocation strain field locally surrounding the dislocation (Harjo *et al.*, 2016). Modified Williamson–Hall (MWH) and modified Warren–Averbach (MWA) methods were used to determine the dislocation density ρ of the powder samples (HajyAkbary *et al.*, 2015). The annealing process heals the dislocations within the microstructure (Jeon *et al.*, 2021; Scardi *et al.*, 2018); a comparison of dislocation density results from as-atomized and annealed samples verified this assertion.

The stochastic nature of the gas-atomization process generates a variety of particle sizes, each of which cools at a rate correlated to its respective diameter. This cooling rate can be quantified by observing the secondary dendrite arm spacing (SDAS) of the microstructure to calculate an apparent grain size. This observed grain interface area can be correlated to the cooling rate experienced by the particle during solidification (Zheng *et al.*, 2009; Sousa *et al.*, 2020). Zheng *et al.* (2009) provide a general equation for SDAS as a function of cooling rate and assert the relationship of decreasing SDAS with increasing cooling rate. Reported values for similar samples range from 10^3 to 10^7 K s^{-1} (Zheng *et al.*, 2009; Sousa *et al.*, 2020; Wiskel *et al.*, 2002; Prasad *et al.*, 2009; Mullis *et al.*, 2013; Gianoglio *et al.*, 2021; Kumar *et al.*, 2022); however, this is highly dependent on the experimental setup. Cooling rate results can be combined with the dislocation density from line profile analysis (LPA) to predict the average misorientation angle between the apparent grains. Electron backscatter diffraction techniques can then be used to quantify and validate these average misorientation angle predictions.

The motivation for this paper is to apply these analysis techniques to discrete particle populations to define the relationship between particle size, cooling rate, dislocation density and average misorientation angle in gas-atomized Al2024 powder.

2. Experimental procedure

2.1. Sample preparation

The gas-atomized Al2024 powder, sourced from Solvus Global, was isolated into two populations, one raw stock and one stock with subsequent annealing treatment. The annealed samples of the Al2024 powder were isothermally held at 490°C for 6 h in an argon atmosphere. These samples were subsequently sifted into distinct powder size ranges using powder sieve sifting techniques. The particle diameter ranges utilized in this experiment include 20–25, 25–32, 32–38, 38–45, 45–53 and 53–63 µm. Both sets of powders were isolated using a DUAL Manufacturing Co. Inc. Model D-4326 sieve shaker with DUAL Manufacturing Co. Inc. ASTM E11 specification mesh screens. The particle isolation was validated using a JEOL Model JSM-7600F field-emission scanning electron microscope, as shown in Fig. 1. The *ImageJ* software (Schneider *et al.*, 2012; https://imagej.net/ij/) was used to isolate and quantify average grain interface areas from the etched cross-section micrographs of particles.

Chemical analysis, as shown in Table 1, was performed by Luvak Laboratories Inc. (Boylston, Massachusetts, USA)

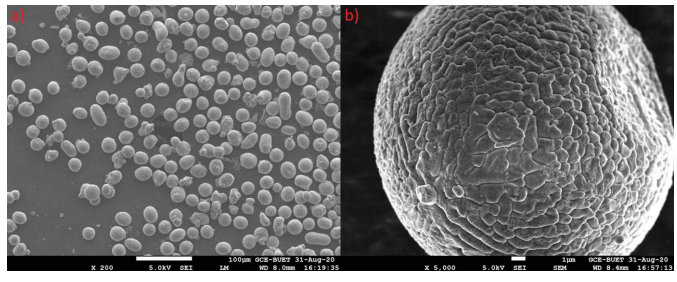


Figure 1
Scanning electron micrographs of Al2024 powder particles showing (*a*) isolated particles within the 20–25 µm diameter range and (*b*) a high-resolution micrograph of a single particle.

electronic reprint

Table 1
Material analysis of Al2024 samples.

Element	Weight percentage (%)
Copper	4.19
Magnesium	1.59
Manganese	0.61
Oxygen	0.026
Silicon	0.003
Aluminium	Balance

using the ASTM E1019-18 and ASTM E1097-12 standards and ASTM E29 rounding methods.

2.2. Synchrotron powder X-ray diffraction

Synchrotron powder X-ray diffraction was performed on beamline 11-ID-C at the Advanced Photon Source (APS), Argonne National Laboratory, Illinois, USA, with a high-energy beam (E = 105.7 keV, λ = 0.1173 Å). Each powder was loaded into a thin-walled amorphous glass capillary of 1 mm outer diameter, the sample configuration recommended for this beamline. This diameter provides sufficient diffracting volume for reliable counting statistics across the full q range, while the thin amorphous wall contributes only a diffuse background signal and no Bragg peaks. Two-dimensional diffraction patterns were collected in transmission (Debye–Scherrer) geometry using a Perkin–Elmer amorphous-silicon area detector with a 1 s exposure and were azimuthally integrated to one-dimensional intensity versus q profiles using the *FIT2D* software (Hammersley, 2016; https://www.esrf.fr/computing/scientific/FIT2D/).

The apparent Bragg peak FWHM is a convolution of both the XRD instrumental broadening effect, $\beta_{\text{instrument}}$, and the broadening effect due to the sample, β_{sample} (Sallez *et al.*, 2015). The instrumental broadening effect was determined by first measuring the appropriate NIST XRD standard reference material (Balzar, 1999): LaB_6, No. SRM660c, produced by NIST, Gaithersburg, Maryland, USA. A curve fit using the Caglioti formula (Caglioti *et al.*, 1958) was used to determine the instrumental broadening as a function of incident angle θ, as shown in equation (1):

$$\text{FWHM}(\theta) = \left[W + V\tan(\theta) + U\tan^2(\theta)\right]^{1/2}. \quad (1)$$

Here, the instrumental peak broadening (expressed as the FWHM of the XRD data of the standard reference material) is a function of θ, with W, V and U representing adjustable parameters utilized during the curve fitting process.

The broadening due to the sample was isolated from instrumental effects using equation (2),

$$\beta^2_{\text{measured}} = \beta_{\text{sample}}\beta_{\text{measured}} + \beta^2_{\text{instrument}}. \quad (2)$$

This isolation is applicable to Voigt function fits to XRD data (Balzar, 1999). The LaB_6 standard was measured in the same 1 mm capillary tubes used for the powder samples, so any broadening from the capillary or sample size is part of the instrumental correction and is removed. Every sample was measured using an identical procedure, so this effect is constant across all of them and does not change the comparison between particle sizes.

2.3. Electron backscatter diffraction characterization

The electron backscatter diffraction (EBSD) samples were embedded in the electrically conductive material Polyfast (manufactured by Struers) at a temperature of 450 K and pressure of 25 kN. These specimens were gently ground with SiC paper and polished, first with a chemically neutral suspension of alumina particles, and then with a colloidal silica suspension (diameter = 100 nm) with pH = 9.8. A Merlin scanning electron microscope by Zeiss with a spatial resolution of 1 nm was used to perform the EBSD measurements with the EBSD system AZtec and detector NordlysMax3 by Oxford. The *CHANNEL5* software (https://nano.oxinst.com; (Oxford Instruments NanoAnalysis, Abingdon, UK) was used to visualize the local misorientation.

3. Results and discussion

3.1. Line profile analysis of X-ray diffraction

The synchrotron diffraction patterns (λ = 0.1173 Å) of as-atomized and annealed Al2024 samples, spanning the first ten face-centered cubic (f.c.c.) Bragg peaks, are shown in Fig. 2 for

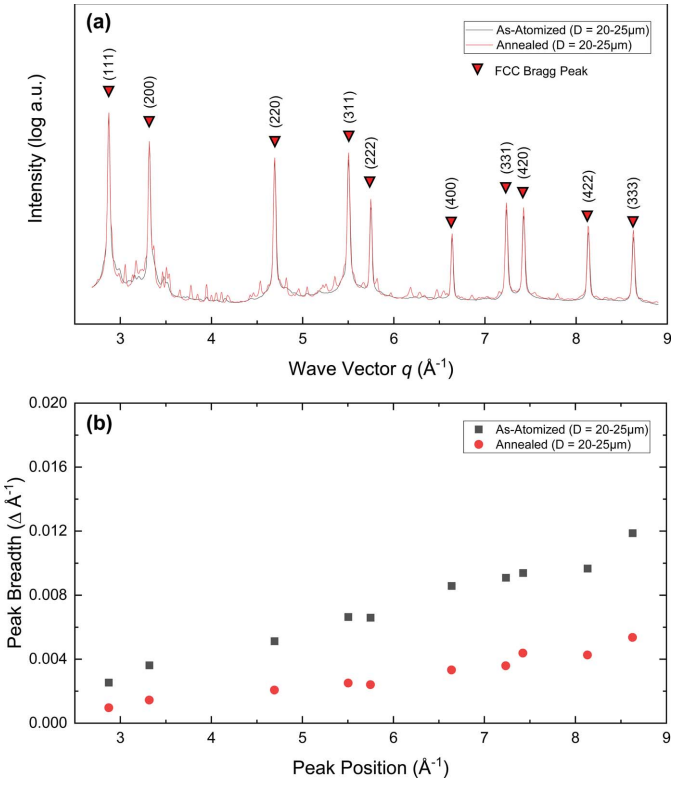


Figure 2
(*a*) XRD patterns of as-atomized and annealed Al2024 powders with particle diameters ranging from 20 to 25 µm plotted on a logarithmic intensity scale. (*b*) Corresponding Bragg peak breadth versus position, illustrating the reduction in lattice strain and defect content, which is further analyzed in the text.

electronic reprint

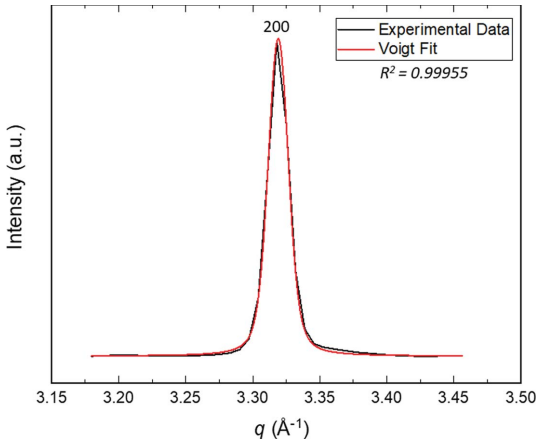


Figure 3
Curve fit of a Voigt function to the 200 Bragg peak of an as-atomized Al2024 20–25 µm diameter sample.

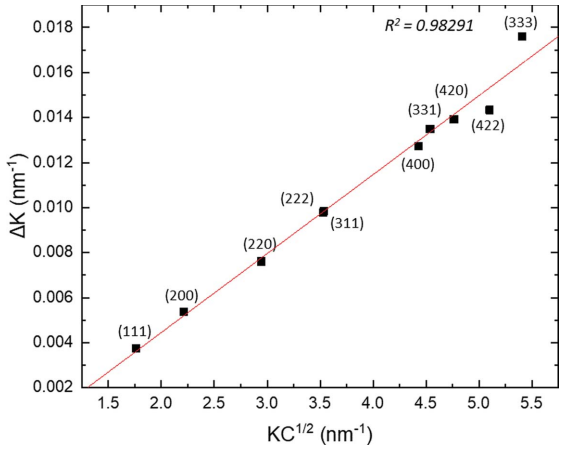


Figure 4
Modified WH plot showing the comparison between Bragg peak FWHM (ΔK) as a function of peak position (K) while accounting for microstrain anisotropy.

the 20–25 µm particle diameter group. The complete experimental scope of this work encompasses additional particle diameter ranges (25–32, 32–38, 38–45, 45–53 and 53–63 µm). Following annealing, several low-intensity Bragg peaks appear that are absent from the as-atomized sample data. These correspond to precipitates formed during the annealing treatment. Their apparent prominence is exaggerated by the logarithmic intensity scale, and they have little influence on the dislocation density results or the conclusions of this work.

To quantify the peak broadening shown in Fig. 2(*b*), individual Bragg peaks were fitted using a Voigt function (Balzar, 1999). An example of this fitting procedure, applied to the 200 reflection, is presented in Fig. 3.

3.1.1. Modified Williamson–Hall method

Once any instrumental broadening effects have been removed, the effects of size and strain can be further isolated using the Williamson–Hall (WH) method (Williamson & Hall, 1953). The classical WH equation explains peak broadening as a sum of the crystallite size and microstrain,

$$\Delta K = \alpha + \varepsilon K. \tag{3}$$

K is the magnitude of the diffraction vector defined by $K = 2\sin(\theta)/\lambda$, with θ the diffraction angle of the centroid of the diffraction peak and λ the wavelength of the incident beam. ΔK is the FWHM of the diffraction peak when plotted using K; it is defined by $\Delta K = 2\cos(\theta)\Delta\theta/\lambda$. α is a factor relating to crystallite size and ε is the microstrain of the atomic lattice.

The MWH method is an improved technique for determining the dislocation density in crystalline materials. It is based on the same principles as the original WH method but uses a more sophisticated model that considers the effects of anisotropic microstrains on different *hkl* reflections. The MWH method to account for dislocation anisotropy (Ungár & Borbély, 1996) is shown in equation (4) and Fig. 4.

$$\Delta K \simeq \frac{0.9}{D} + \left(\frac{\pi M^2 b^2}{2}\right)^{1/2} \rho^{1/2} K \overline{C}^{1/2} + O\left(K^2 \overline{C}\right), \tag{4}$$

where ΔK is again the FWHM of the diffraction peak, D is the coherent crystallite domain size for diffraction, M is a dimensionless parameter depending on the dislocation density and outer cut-off radius of the dislocations, b is the magnitude of the Burgers vector, ρ is the dislocation density, K is the centroid of the diffraction peak, $\overline{C}$ is the average contrast factor of the dislocations, and O is all the higher-order terms.

The primary modification to this method was the inclusion of the $\overline{C}$ term, a method of accounting for anisotropy (Simm, 2018). This term can be written in terms of Miller indices,

$$\overline{C}_{hkl} = \overline{C}_{h00}(1 - qH^2). \tag{5}$$

$\overline{C}_{h00}$ is the average contrast factor corresponding to the $h00$ reflections (identified through the elastic constants of the material) (Ungár *et al.*, 1999), q is the dislocation character, a description of the microstrain anisotropy due to the edge or screw character of the dislocations (Ungár *et al.*, 1999), and H^2 is an orientation parameter described as

$$H^2 = \frac{h^2k^2 + h^2l^2 + k^2l^2}{(h^2 + k^2 + l^2)^2}. \tag{6}$$

The $\overline{C}_{h00}$ term of equation (5) may be calculated using equation (7) (Ungár *et al.*, 1999),

$$\overline{C}_{h00} = a\left[1 - \exp\left(\frac{A_i}{b}\right)\right] + cA_i + d. \tag{7}$$

a, b, c and d are parameters depending on the dislocation character, the crystal structure and the ratio of c_{12} to c_{44}, as described by Ungár *et al.* (1999), and A_i is the elastic anisotropy, which can be defined by the elastic constants c_{11}, c_{12} and c_{44}:

$$A_i = \frac{2c_{44}}{(c_{11} - c_{12})}. \tag{8}$$

electronic reprint

Experimental results of Al2024 elastic constants from the literature (Zeng & Ericsson, 1996) were used in this analysis: $c_{11} = 10.820 \times 10^{10}$ Pa, $c_{12} = 5.939 \times 10^{10}$ Pa and $c_{44} = 2.926 \times 10^{10}$ Pa.

3.1.2. Modified Warren–Averbach method

The Warren–Averbach (WA) method uses the Fourier coefficients of XRD profiles to determine dislocation density (Ungár, 2001; Ungár *et al.*, 1998). The WA equation can be modified to account for the average contrast factor, as shown in equation (9) and Fig. 5:

$$\ln[A(L)] \simeq \ln\left[A^S(L)\right] - \frac{\rho\pi b^2 L^2}{2}\ln\left(\frac{R_e}{L}\right)\left(K^2\overline{C}\right) + Q\left(K^4\overline{C}^2\right). \quad (9)$$

A is the real part of the Fourier coefficient, A^S is the size Fourier coefficient (Shintani & Murata, 2011) and L is the Fourier length defined as $L = na_3$, where a_3 is $\lambda/[2(\sin\theta_2 - \sin\theta_1)]$, n is an integer starting from zero and $(\theta_2 - \theta_1)$ is the θ range for the XRD profile. ρ is the dislocation density, b is the magnitude of the Burgers vector, R_e is the effective outer cut-off radius of dislocations, K is the centroid of the diffraction peak, C is the contrast factor and Q is the collection of quadratic terms.

In the concluding step of the MWA method, the dislocation density is determined using equation (9). These results are shown in Table 2 and Fig. 6. The error bounds of the particle sizes of the powder were estimated using the standard deviation of a normal distribution within the particle size range. The reported dislocation density error bounds were obtained by propagating the standard error of the regression slope from which the dislocation density is extracted, consistent with the precision generally reported for similar line profile analyses.

The heat treatment applied to the Al2024 powder samples allowed the dislocations present within the microstructure of the as-atomized samples to move and annihilate, leading to a reduced dislocation density. The results shown in Fig. 6 indicate that the resulting dislocation density of the as-atomized samples is due to differences in solidification histories across varying particle diameters. The annealing process showed that the dislocations can be adequately healed such that the trend across the particle diameter range is effectively removed.

Table 2
Al2024 dislocation density results.

Particle diameter (μm)	As-atomized sample dislocation density (10^{14} m^{-2})	Annealed sample dislocation density (10^{14} m^{-2})
22.5 ± 1.4	7.4 ± 1.3	2.3 ± 0.4
28.5 ± 2.0	6.7 ± 1.2	2.2 ± 0.4
35.0 ± 1.7	5.3 ± 1.0	1.3 ± 0.2
41.5 ± 2.0	6.1 ± 1.1	4.0 ± 0.7
49.0 ± 2.3	5.0 ± 0.9	3.1 ± 0.6
58.0 ± 2.9	3.1 ± 0.6	2.0 ± 0.4

The dislocation density of as-atomized and annealed Al2024 powders has been investigated as a function of particle size and solidification history. The as-atomized samples demonstrated a trend of decreasing dislocation density with increasing particle size. The solidification process of the larger atomized particles involved a lower cooling rate and experienced less undercooling than the smaller atomized particles. The dislocation densities found for all samples ranged between 10^{14} and 10^{15} m^{-2}, which is consistent with other studies of dislocation density of similarly sized particles (Jeon *et al.*, 2021; Azersky *et al.*, 2023; Prasad *et al.*, 2021; Brown *et al.*, 2017). The annealed Al2024 powder samples demonstrated lower dislocation densities than the as-atomized Al2024 powder samples across all particle size ranges. Additionally, the annealed Al2024 samples showed little to no trend of dislocation density across the span of particle sizes, which experienced a range of different cooling rates and undercoolings during solidification.

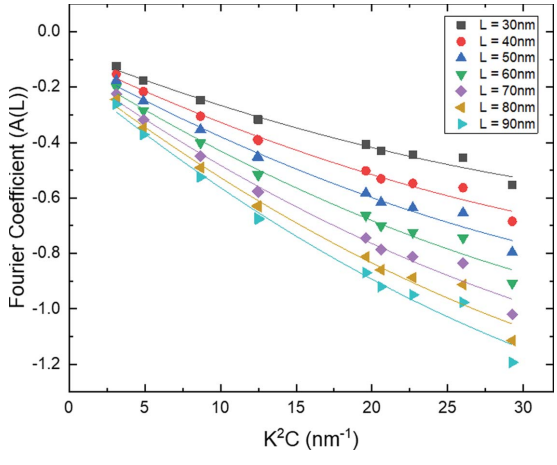


Figure 5
Modified WA plot showing the Fourier coefficient $A(L)$ versus K^2C for the as-atomized 20–25 μm diameter Al2024 sample.

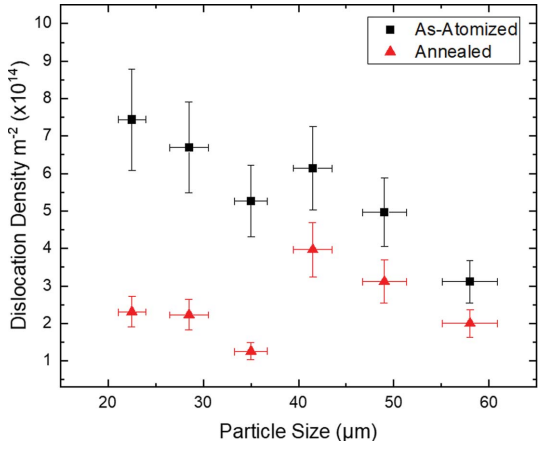


Figure 6
Dislocation density results for both the as-atomized and annealed Al2024 powder samples for particle size ranges 20–25, 25–32, 32–38, 38–45, 45–53 and 53–63 μm.

electronic reprint

3.2. Cooling rate correlation

The correlation used by Sousa *et al.* (2020) in an experiment using gas-atomized aluminium alloys was utilized to approximate the cooling rate of the samples using the results from the grain interface area analysis. The SDAS was approximated by the apparent grain diameter obtained from the process shown in Fig. 7 using equation (10),

$$\lambda_x = \lambda_0 \left(\frac{dT}{dt} \right)^n, \tag{10}$$

with results given in Table 3. In equation (10), λ_x is the SDAS (in micrometres), λ_0 and n are material-specific constants [values of λ_0 = 86.741 µm and n = −0.33 were used here, as provided by Sousa *et al.* (2020) using the *JMatPro* software (Saunders *et al.*, 2003; https://www.sentesoftware.co.uk/), and dT/dt is the cooling rate (in units of K s^{-1}).

The resulting plot of dislocation density versus cooling rate, as shown in Fig. 8, indicates a trend of increasing dislocation densities with increased cooling rates. As previously mentioned, the particle diameter is correlated with cooling rate, so the results shown in Fig. 8 are consistent with the results shown in Fig. 6. High cooling rates promote the generation of a higher dislocation density due to the insufficient time for dislocation annihilation processes to occur. Analysis of larger particle size ranges in this experiment revealed larger apparent grain sizes and lower dislocation densities relative to their smaller counterparts. According to these results, dislocation annihilation was more effective in larger samples with larger grain interface areas.

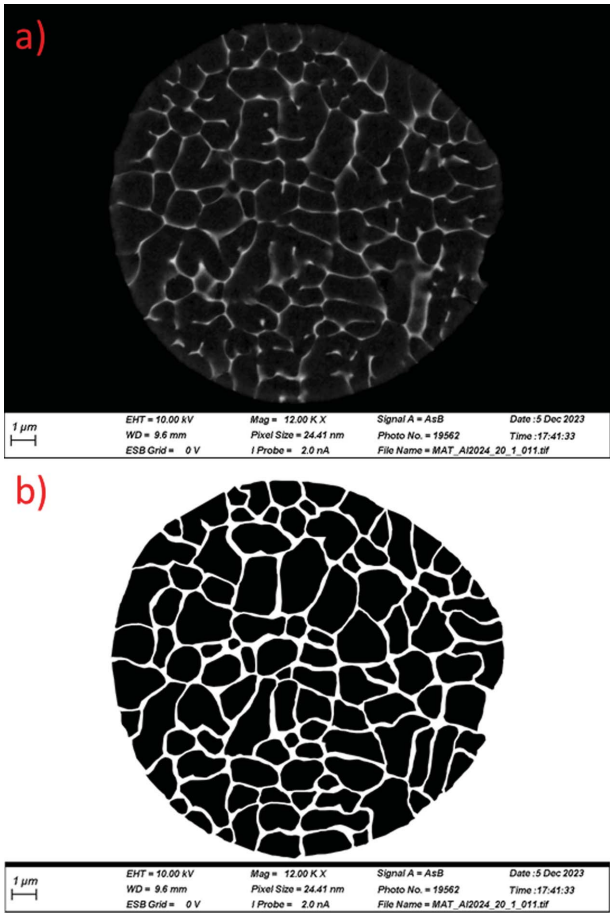


Figure 7
Grain interface area identification and characterization example for an as-atomized Al2024 20–25 µm diameter particle. (*a*) Unprocessed micrograph of an etched cross section of the interior of a particle and (*b*) isolation of apparent grains used in the *ImageJ* particle analysis.

Table 3
Al2024 grain interface size and cooling rate approximation.

Particle diameter (µm)	Grain interface diameter (µm)	Approximate cooling rate (K s^{-1})	Dislocation density (10^{14} m^{-2})
20–25	1.65	164000	7.4 ± 1.3
25–32	1.71	147000	6.7 ± 1.2
32–38	1.90	107000	5.3 ± 1.0
38–45	1.84	118000	6.1 ± 1.1
45–53	1.82	122000	5.0 ± 0.9
53–63	3.20	22000	3.1 ± 0.6

3.3. Local misorientation angle determination

As a check of the impact of dislocation concentration on microstructure, EBSD characterization for as-atomized Al2024 samples with particle diameters between 20 and 63 µm was performed to measure average local misorientation angles of the same samples used in XRD analysis, as shown in Fig. 9. Local misorientation angles at a resolution of 0.05° were obtained utilizing a step size of 0.1 µm. The calculation of the map uses a filter of 5 × 5 pixels. For every pixel in the map the orientation difference compared with the average orientation of the 24 surrounding pixels is calculated and assigned to the map using a color coding from blue to green to yellow to red (5°), while unmapped pixels are shown as black in Fig. 9.

The local misorientation angle measured by EBSD conforms to a log-normal distribution. For a distribution of this shape, the geometric mean, which is equivalent to the median of the log-normal fit, is a more representative measure of the average misorientation than the arithmetic mean

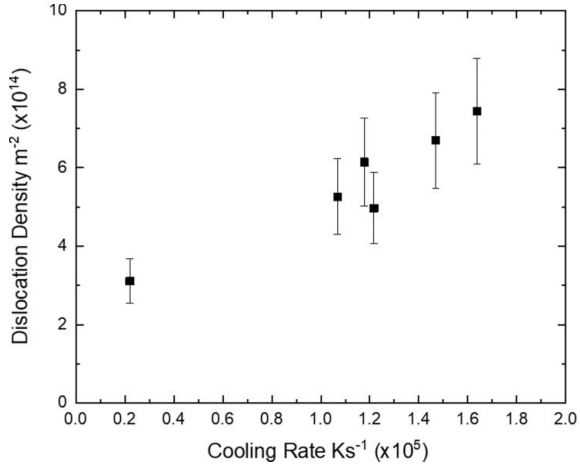


Figure 8
Dislocation density of the as-atomized Al2024 samples as a function of cooling rate.

electronic reprint

[shown in Figs. 9(*g*), 9(*h*) and 9(*i*)], which is inflated by the high-angle tail of the curve. The geometric means of the measured misorientation angles were $0.95^{0.35}_{-0.25}$, $0.89^{0.31}_{-0.23}$ and $0.74^{0.33}_{-0.22}$ degrees for the 20–25, 38–45 and 53–63 μm particles, respectively. This angle decreased with increasing particle size.

The misorientation angle was also predicted independently from the dislocation density. The dislocation density and grain size were first used to estimate the dislocation spacing, which then allowed for the calculation of the predicted misorientation angle (Read & Shockley, 1950). The predicted angles were $0.83^\circ \pm 0.14^\circ$, $0.77^\circ \pm 0.13^\circ$ and $0.68^\circ \pm 0.13^\circ$ for the 20–25, 38–45 and 53–63 μm particles, respectively. This angle also decreased with increasing particle size.

The measured and predicted misorientation angles are compared with the dislocation density as a function of particle size in Fig. 10, with the dislocation density shown on a separate *y* axis. All three quantities follow the same trend, decreasing with increasing particle size. The agreement between the independently measured and predicted misorientation angles, together with their shared dependence on particle size, links the dislocation density determined by XRD to the grain misorientation observed by EBSD.

The local misorientation obtained from EBSD reflects only the geometrically necessary dislocations, while the XRD analysis measures the total density of both geometrically necessary and statistically stored dislocations. The two

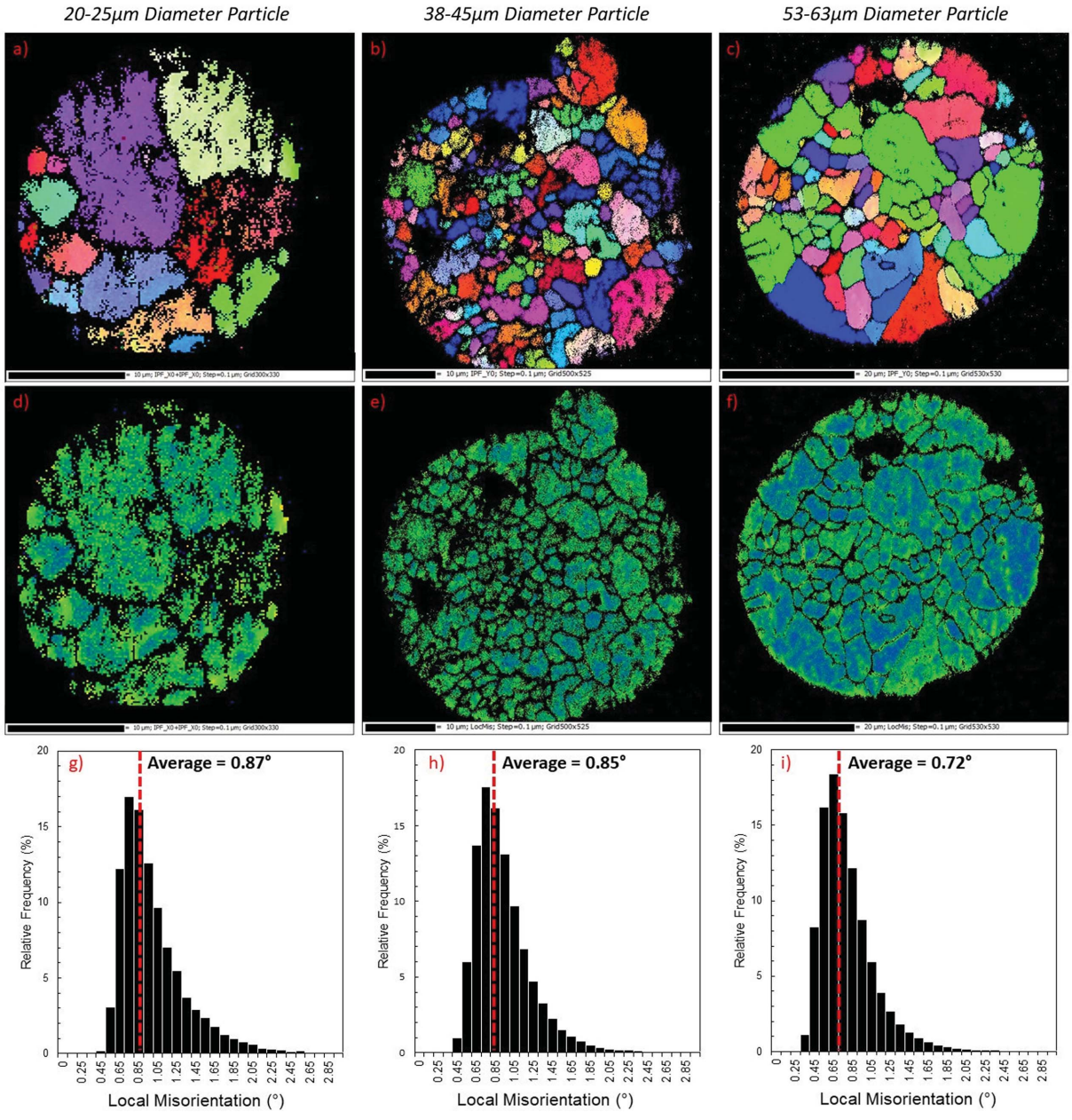


Figure 9
(*a*)–(*c*) EBSD micrographs for as-atomized Al2024 samples with particle diameter ranges of 20–25, 38–45 and 53–63 μm, respectively. (*d*)–(*f*) Misorientation angle between individual grains. (*g*)–(*i*) Histograms of the relative frequencies of local misorientations.

electronic reprint

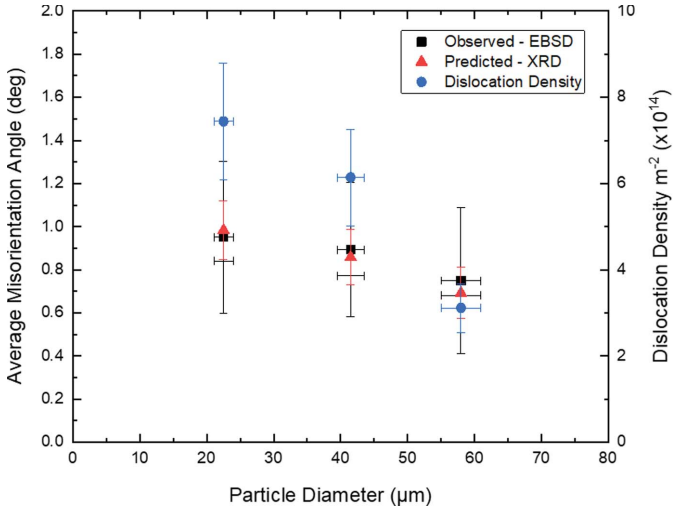


Figure 10
Comparison between the observed average misorientation angle (black squares) from EBSD analysis, the predicted average misorientation angle (red triangles) using both LPA of the XRD data and grain size from metallographic examination, and dislocation density (blue circles) for as-atomized Al2024 samples with particle diameter ranges of 20–25, 38–45 and 53–63 μm.

measurements are therefore not directly equivalent. The meaningful result is the shared trend, with both decreasing as the particle size increases, rather than the absolute values, and the comparison is best viewed as a consistency check between independent methods.

4. Conclusion

This study has mapped the dislocation content of gas-atomized Al2024 powder across a range of particle sizes and related it to solidification history. LPA of the XRD data from as-atomized samples and subsequently annealed samples revealed a clear trend of decreasing dislocation density with increasing particle size in the as-atomized condition, and a uniform lower density across all sizes after annealing. This confirms that the as-atomized dislocation density is induced by rapid solidification and can be largely recovered via heat treatment. The higher surface-to-volume ratio of smaller particles suggests faster cooling at smaller sizes, and metallography of the solidification substructure provides physical evidence of this increased cooling rate for smaller particle sizes within the sample population. Average misorientation angles predicted from the dislocation density and grain size were found to follow the same trend as the values measured by EBSD, linking the XRD results to an independent measurement of the microstructure. The dislocation density rose with cooling rate, showing that the differences in defect content between particles reflect their differing solidification histories.

While previous line profile studies of Al2024 examined bulk material, this work is the first to quantify the solidification-induced dislocation density of the as-atomized powder. Al2024 was used here as a well characterized model alloy, and the contribution of this work is the physical relationship it establishes between particle size, cooling rate, dislocation density and grain misorientation during rapid solidification, demonstrated through X-ray LPA and confirmed by EBSD. These relationships describe the defect structure produced during rapid solidification of gas-atomized powder, and they are important both for the study of solidification and for industrial applications where the powder is used without necessarily being fully remelted, for example in cold-spray additive manufacturing. Applying the same analysis methods to additional alloys, over a wider range of cooling rates, would test how generally these relationships hold. As applications that rely on rapid solidification become more prominent, this approach provides a direct method of relating solidification history to defect structure.

Acknowledgements

Author contributions are as follows: conceptualization of the scope of the work, DM; sample preparation, sample measurements and dislocation density analysis, CA and SJ; provision of the Al2024 samples, CW; EBSD analysis, MK; principal investigator and provision of funding for portions of the work, DM; revision of the final version of the manuscript, CA and DM.

Conflict of interest

The authors declare that there are no conflicts of interest regarding the publication of this manuscript.

Data availability

The data supporting the findings of this study are available from the corresponding author upon request.

Funding information

The following funding is acknowledged: National Aeronautics and Space Administration (grant Nos. NNX17AH41G, 80NSSC19K0256 and 80NSSC23K0573 to DM).

References

Azersky, C., Jeon, S., Settens, C., Fakhrul, M. & Matson, D. (2023). *IOP Conf. Ser. Mater. Sci. Eng.* **1281**, 012033.
Balzar, D. (1999). *Voigt-Function Model in Diffraction Line-Broadening Analysis*, edited by R. L. Snyder, J. Fiala & H. J. Bunge, Vol. 1, pp. 94–126. International Union of Crystallography.
Brown, D. W., Adams, D. P., Balogh, L., Carpenter, J. S., Clausen, B., King, G., Reedlunn, B., Palmer, T. A., Maguire, M. C. & Vogel, S. C. (2017). *Metall. Mater. Trans. A* **48**, 6055–6069.
Caglioti, G., Paoletti, A. & Ricci, F. P. (1958). *Nucl. Instrum.* **3**, 223–228.
Gallagher, C., Kerr, E. & McFadden, S. (2023). *Powder Technol.* **429**, 118873.
Gianoglio, D., Ciftci, N., Armstrong, S., Uhlenwinkel, V. & Battezzati, L. (2021). *Metall. Mater. Trans. A* **52**, 3750–3758.
HajyAkbary, F., Sietsma, J., Böttger, A. J. & Santofimia, M. J. (2015). *Mater. Sci. Eng. A* **639**, 208–218.

electronic reprint

Hammersley, A. P. (2016). *J. Appl. Cryst.* **49**, 646–652.
Harjo, S., Kawasaki, T., Gong, W. & Aizawa, K. (2016). *J. Phys. Conf. Ser.* **746**, 012046.
Henein, H., Uhlenwinkel, V. & Fritsching, U. (2017). *Metal Sprays and Spray Deposition*. Springer International Publishing.
Jeon, S., Liu, X., Azersky, C., Ren, J., Zhang, S., Chen, W., Hyers, R. W., Costa, K., Kolbe, M. & Matson, D. M. (2021). *Materialia* **18**, 101161.
Kumar, G. S., Sateshwar, M., Sharma, A. R., Palit, M., Sarkar, R., Ghosal, P. & Rao, G. A. (2022). *J. Alloys Compd.* **909**, 164772.
Martinez-Garcia, J., Leoni, M. & Scardi, P. (2009). *Acta Cryst.* A**65**, 109–119.
Mullis, A. M., Farrell, L., Cochrane, R. F. & Adkins, N. J. (2013). *Metall. Mater. Trans. B* **44**, 992–999.
Pekok, M. A., Setchi, R., Ryan, M., Han, Q. & Gu, D. (2021). *Int. J. Adv. Manuf. Technol.* **112**, 175–192.
Prasad, A., Mosbah, S., Henein, H. & Gandin, C.-A. (2009). *ISIJ Int.* **49**, 992–999.
Prasad, K., Obana, M., Ito, A. & Torizuka, S. (2021). *Mater. Charact.* **179**, 111379.
Read, W. T. & Shockley, W. (1950). *Phys. Rev.* **78**, 275–289.
Sallez, N., Boulnat, X., Borbély, A., Béchade, J. L., Fabrègue, D., Perez, M., de Carlan, Y., Hennet, L., Mocuta, C., Thiaudière, D. & Bréchet, Y. (2015). *Acta Mater.* **87**, 377–389.
Saunders, N., Guo, U. K. Z., Li, X., Miodownik, A. P. & Schillé, J. (2003). *JOM* **55**, 60–65.
Scardi, P., Ermrich, M., Fitch, A., Huang, E.-W., Jardin, R., Kuzel, R., Leineweber, A., Mendoza Cuevas, A., Misture, S. T., Rebuffi, L. & Schimpf, C. (2018). *J. Appl. Cryst.* **51**, 831–843.
Schneider, C. A., Rasband, W. S. & Eliceiri, K. W. (2012). *Nat. Methods* **9**, 671–675.
Shintani, T. & Murata, Y. (2011). *Acta Mater.* **59**, 4314–4322.
Simm, T. H. (2018). *Crystals (Basel)* **8**, 212.
Sousa, B. C., Walde, C., Champagne, V. K., Nardi, A. T., Sisson, R. D. & Cote, D. L. (2020). *Coatings* **10**, 1035.
Tong, X., Zhang, H. & Li, D. Y. (2015). *Sci. Rep.* **5**, 8459.
Ungár, T. (2001). *Mater. Sci. Eng. A* **309–310**, 14–22.
Ungár, T. & Borbély, A. (1996). *Appl. Phys. Lett.* **69**, 3173–3175.
Ungár, T., Dragomir, I., Révész, Á. & Borbély, A. (1999). *J. Appl. Cryst.* **32**, 992–1002.
Ungár, T., Ott, S., Sanders, P. G., Borbély, A. & Weertman, J. R. (1998). *Acta Mater.* **46**, 3693–3699.
Williamson, G. K. & Hall, W. H. (1953). *Acta Metall.* **1**, 22–31.
Wiskel, J. B., Navel, K., Henein, H. & Maire, E. (2002). *Can. Metall. Q.* **41**, 193–204.
Zeng, X. H. & Ericsson, T. (1996). *Acta Mater.* **44**, 1801–1812.
Zhan, J. Z., Zhang, G., Ma, J. F., Liu, Z. & Song, J. (2021). *Strength Mater.* **53**, 610–618.
Zhang, Z., Ódor, É., Farkas, D., Jóni, B., Ribárik, G., Tichy, G., Nandam, S. H., Ivanisenko, J., Preuss, M. & Ungár, T. (2020). *Metall. Mater. Trans. A* **51**, 513–530.
Zheng, B., Lin, Y., Zhou, Y. & Lavernia, E. J. (2009). *Metall. Mater. Trans. B* **40**, 995–1004.

electronic reprint